Petroleum Science 23 (2026) 7522–7537

Contents lists available at ScienceDirect

Petroleum Science

journal homepage: www.keaipublishing.com/en/journals/petroleum-science

Original Paper

Electrical resistivity tomography visualization of core-scale evolution to reveal the impact of lithologic heterogeneity on gas hydrate formation in marine sediments

Xi-Xi Lan [a,b], Qing-Tao Bu [c,*], Xiao-Li Hong [d], Jin-Huan Zhao [d,**], Qiang Chen [c], Yuan-Yuan Zhang [b], Chang-Chun Zou [b], Guang-Bo Xu [e]

[a] Faculty of Electric Power Engineering, Kunming University of Science and Technology, Kunming, 650500, Yunnan, China
[b] School of Geophysics and Information Technology, China University of Geosciences, Beijing, 100083, China
[c] Key Laboratory of Gas Hydrate, Ministry of Natural Resources, Qingdao Institute of Marine Geology, Qingdao, 266237, Shandong, China
[d] Qingdao National Marine Equipment Quality Inspection Group Co., Ltd., Qingdao, 266237, Shandong, China
[e] PetroChina Huabei Oilfield Company, Renqiu, 062550, Hebei, China

ARTICLE INFO

Article history:
Received 28 August 2025
Received in revised form
26 November 2025
Accepted 20 April 2026
Available online 24 April 2026

Edited by Min Li

Keywords:
Gas hydrate
Electrical resistivity tomography
Hydrate growth pattern
Resistivity feature
Simulation experiment

ABSTRACT

Natural gas hydrate represents a significant clean energy resource, whose formation and distribution are critically controlled by sediment heterogeneity. While electrical resistivity tomography (ERT) technology effectively detects hydrate-induced resistivity anomalies, current understanding is heavily biased towards sandy systems, with fine-grained muddy sediments remaining poorly characterized. Utilizing a self-developed ERT experimental system, this study conducted multi-cycle hydrate formation experiments on representative the South China Sea sediments: sea sand and clayey silt. The representative results reveal fundamentally distinct hydrate formation and evolution patterns governed by sediment type. In sea sand, pore water prevents gas from entering pore, leading to localized hydrate enrichment near the gas source. However, the fracture network in muddy sediments is conducive to methane migration, allowing hydrates to form at greater distances. Sediment heterogeneity dictates hydrate distribution and evolution by controlling pore structure and gas-water behavior. Moreover, within the pore space, hydrate growth follows a selective pattern driven by methane concentration gradients, with areas rich in methane supply becoming focal points for hydrate formation. This study elucidates the core-scale evolutionary characteristics of hydrate formation in heterogeneous marine sediments via ERT visualization. The identified distinct resistivity signatures and formation mechanisms provide a critical basis for interpreting hydrate occurrence, formation and exploration.
© 2026 The Authors. Publishing services by Elsevier B.V. on behalf of KeAi Communications Co. Ltd. This is an open access article under the CC BY license (http://creativecommons.org/licenses/by/4.0/).

1. Introduction

Natural Gas Hydrate (NGH) is a sub-stable compound formed by water molecules wrapped around methane and other gas molecules in a cage-like crystal structure constructed by hydrogen bonding, and its thermodynamic stability is strictly controlled by temperature-pressure phase equilibrium boundary conditions, which has become the limelight of the global energy vision (Sloan Jr and Koh, 2007). Global assessments confirm that NGH reserves represent a methane resource of unparalleled scale, substantially surpassing the combined reserves of conventional oil and natural gas. Meanwhile, 1 m^3 NGH can release 164–180 m^3 methane, and this high energy density characteristic and its clean attribute of near-zero particulate emissions after combustion make it a core research topic for global energy transition strategies (Sloan Jr, 2003; Stanwix et al., 2018; Metaxas et al., 2019; Atig et al., 2020; Fan et al., 2025). However, the enormous development potential of NGH contrasts sharply with its complex occurrence conditions. They are not evenly distributed on the seabed, but are strongly controlled by the physical and chemical properties of sediments.

* Corresponding author.
** Corresponding author.
E-mail addresses: bqt881110@163.com (Q.-T. Bu), zhaojinhuan99@yeah.net (J.-H. Zhao).
Peer review under the responsibility of China University of Petroleum (Beijing).

https://doi.org/10.1016/j.petsci.2026.04.034
1995-8226/© 2026 The Authors. Publishing services by Elsevier B.V. on behalf of KeAi Communications Co. Ltd. This is an open access article under the CC BY license (http://creativecommons.org/licenses/by/4.0/).

Approximately 78% of the global NGH resources are distributed within unconsolidated marine sediments along continental margins, where muddy and sandy sediments constitute 53% and 34% of these reservoirs, respectively, which have strong sediment heterogeneity (Lu et al., 2019; Boswell et al., 2020; Zhu et al., 2024). These sediment types exhibit fundamentally distinct physicochemical characteristics, including mineral composition, particle size distribution, permeability, pore structure, specific surface area, cation exchange capacity, organic matter content, and moisture retention capacity. These intrinsic sedimentological differences directly dictate the mechanisms and efficiency of gas transport and water migration, the preferred locations and morphology of hydrate formation and the consequent spatial distribution patterns and saturation levels of hydrates within the sediment matrix, which collectively govern hydrate synthesis kinetics and their corresponding electrical responses (Murray, 2007; Doi et al., 2019; Lei and Seol, 2009; Shi et al., 2022). However, the formation mechanism and morphological differences of hydrates in sedimentary environments remain poorly understood, despite their widespread occurrence in both sandy and muddy sediments. Further systematic and in-depth research is urgently needed to elucidate how the heterogeneity of sedimentary environments influences the formation mechanism and morphological variations of hydrates.

Anomalous changes in resistivity can be used to identify hydrate-bearing reservoirs, estimate hydrate saturation and monitor reservoir changes. The formation of NGH within sediment pore spaces displaces conductive pore water with highly resistive hydrate crystals, leading to a substantial and measurable increase in bulk sediment resistivity (Spangenberg and Kulenkampff, 2006; Lee and Collett, 2006). Sediment heterogeneity fundamentally determines the distribution pattern of hydrates, which in turn dictates the resistivity characteristics. In highly permeable sandy sediments, hydrates typically form as pore-filling particles within intergranular spaces, leading to relatively uniform reductions in pore connectivity and correspondingly more uniform increases in bulk resistivity. This generally conforms to models such as Archie's law. In contrast, clayey silt deposits often result in more complex and heterogeneous hydrate formation patterns (Lee et al., 2013). Consequently, extrapolating sandy sediment models to muddy systems is inadequate for understanding reservoir formation mechanisms or guiding exploration. Therefore, elucidating how specific sediment types govern distinct hydrate formation pathways and resultant resistivity signatures is essential for building accurate reservoir models and developing targeted exploration strategies in heterogeneous marine environments.

Resistivity is sensitive not only to hydrate volume but also to the specific morphology and spatial distribution of hydrates. Electrical Resistivity Tomography (ERT) has emerged as a particularly promising geophysical methodology to address the critical characterization deficit surrounding hydrate reservoir dynamics. In particular, ERT technique is capable of reflecting the dynamic electrical spatial distribution information of the core by integrating the spatial resolution principle of medical computerized tomography (CT) with geophysical inversion algorithms, which breaks the limitations of traditional single-point measurements (Bosch et al., 2016; Bergmann et al., 2017; Liu et al., 2023). The technique's advantages have cemented its utility across diverse fields, including operational simplicity, rapid data acquisition, non-destructive nature, cost-effectiveness, and suitability for long-term monitoring (Wehrer and Slater, 2015; Pleasants et al., 2022; Perrone et al., 2014; Merritt et al., 2016). It is able to visually compare and elucidate the spatiotemporal evolution of hydrate formation within two representatives yet fundamentally different marine sediments in the South China Sea: sea sand and clayey silt. In the future, ERT is expected to be a key geophysical tool for hydrate exploration, realizing real-time monitoring of reservoir. Currently, in the field of hydrates, several scholars have successfully realized ERT monitoring measurements during the synthesis of hydrates in brine-containing sediment systems, simulated and monitored processes such as hydrate nucleation and micro-crystallization, and explained the nonhomogeneous nature of the hydrate generation process based on the experimental results (Priegnitz et al., 2015; Li et al., 2022; G. Zhao et al., 2022). However, research efforts remain overwhelmingly skewed towards coarse-grained sandy systems, and there is a lack of studies on muddy sediments with finer grain size.

This paper focuses on the electrical response differences between sand and mud sediments during hydrate synthesis. And a systematic comparative experimental study is designed based on ERT device. The study takes sea sand and clayey silt from typical sea areas in the South China Sea as experimental media, and carries out replicate hydrate synthesis experiments in a high-pressure, low-temperature reactor to simulate the conditions of the marine environment, respectively. Sediment electrical resistance data is real-time obtained by distributed electrode arrays. Then, the resistivity image is reconstructed by combining the Gaussian Newton iterative method, and the time series electrical resistance dataset is transformed into a spatial two-dimensional resistivity distribution image. Ultimately, the visualization and monitoring of the hydrate synthesis process is realized. It reveals the electrical dynamics of the interior during the experiments, and discusses the differences in the distribution and pattern of hydrate growth in these two sediments. These formation mechanisms offer a vital foundation for advancing reservoir formation theory and optimizing exploration in heterogeneous submarine settings.

2. Method and experiments

2.1. Theory of electrical resistivity tomography

The ERT technique, as a non-invasive visualization technique of the internal structure utilizes the difference of electrical conductivity between different media to real-time monitor changes of target media, which is similar to medical CT technology (Daily et al., 1992; Perrone et al., 2014; Adebayo et al., 2017). This technique works by injecting an electric current into the target media and measuring the potential at the boundary. Specifically, due to the significant resistivity difference between the target medium and its surroundings, the internal potential will be adjusted accordingly when the current passes through, further leading to significant fluctuations in the voltage at the boundary (Dickin and Wang, 1996; Knackstedt et al., 2007; Balasco et al., 2022). It can deduce the specific distribution of conductivity inside the medium by analyzing the changes in the boundary voltage. With the help of mathematical modeling and image reconstruction technology, a high-precision 2D and even 3D resistivity distribution images in real time will be reconstructed. Thus, the spatial distribution of the medium, can be accurately characterized (Fig. 1) (Johnson, 2011; Priegnitz et al., 2013). When sediments contain hydrates, the factors affecting the variation of internal electric fields become complex. These factors contain the specific gas species that promote hydrate generation, the level on salinity of the fluid in the depositional environment, the saturation state of the hydrate and its specific spatial distribution, and so on.

2.2. Method for resistivity image reconstruction

Image reconstruction is the core of ERT technology, which is also known as ERT inverse problem. According to the specific computational process, dozens of algorithms have appeared,

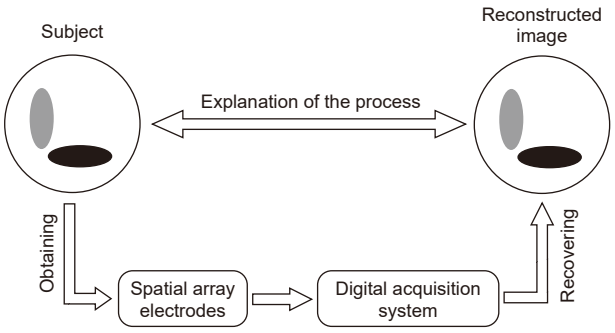


Fig. 1. Components of an electrical resistivity tomography system.

which can be divided into iterative algorithms and non-iterative algorithms (Wedderburn, 1974; Loke and Dahlin, 2002). The ERT inverse problem solution satisfies the following equation:

$$\sigma = S \cdot U \tag{1}$$

where U denotes the voltage data measured on the electrode at the boundary, S denotes the sensitivity matrix which characterizes the mapping relationship between U and the reconstructed image, and σ denotes the reconstructed conductivity distribution.

From the "soft field" property of the electric field, it is known that there is a nonlinear relationship between the measured voltage and the conductivity distribution. Meanwhile, due to the limited number of electrodes, the information collected from the boundary electrodes is relatively scarce compared to the complexity of the conductivity distribution inside the target area. This lack of information directly leads to the so-called "ill-posed equation" problem. Therefore, the ERT inverse problem is a highly nonlinear ill-posed problem, which is difficult to solve, and it can be considered to convert it into an optimal solution of the objective function.

$$F = \operatorname{argmin}\left(\frac{1}{2}\|S \cdot U - \hat{\sigma}\|\right) \tag{2}$$

For the image reconstruction task of ERT, a Gauss-Newton iterative method is adopted. This method cleverly integrates the regularization matrix with the introduction of parameters, aiming at obtaining a more stable and rapidly converging solution. The Gauss-Newton iterative method is essentially a solution technique for nonlinear models, which utilizes a Taylor series expansion to locally linearize the approximation of the nonlinear problem. The regression coefficients are subsequently adjusted iteratively to minimize the sum of squares of the residuals, which effectively solve the complex nonlinear regression problem (Razafindratsima and Lataste, 2014; Najafabadipour and Kamali, 2017). In summary, this method demonstrates significant advantages in constructing and solving the objective function. The objective function can be expressed as:

$$F(m) = \frac{1}{2}\|f(m) - U\|^2 + \lambda R(m) \tag{3}$$

where m denotes the parameter vector of the model, which in this case refers to the resistivity distribution, $f(m)$ denotes the data vector predicted by the model, representing a nonlinear function of the model parameter m. λ denotes the regularization parameter, which is used to balance the weights between the data fit and the regularization term, and $R(m)$ denotes the regularization term, which is used to introduce a priori knowledge of the solution.

The Gauss-Newton iterative method updates the model parameters m by iteratively solving the linearized objective function. It usually directly uses the transpose of the Jacobi matrix multiplied by itself to approximate the Hessian matrix avoiding overly complex calculations ($\mathbf{J}_k^{\mathrm{T}}\mathbf{J}_k$, $\mathbf{J}$ is the Jacobian matrix of f over m). There are:

$$m_{k+1} = m_k + \Delta m_k \tag{4}$$

$$F(m_{k+1}) = \frac{1}{2}\|f(m_k + \Delta m_k) - U\|^2 + \lambda R(m_k + \Delta m_k) \tag{5}$$

where Δm_k is the update quantity obtained by solving the following linear equation:

$$\left(\mathbf{J}_k^{\mathrm{T}}\mathbf{J}_k + \lambda\mathbf{C}\right)\Delta m_k = -\mathbf{J}_k^{\mathrm{T}}\left(f(m_k) - U\right) \tag{6}$$

where $\mathbf{J}_k$ is the Jacobi matrix at m_k and $\mathbf{C}$ is the matrix associated with the regularization term $R(m)$.

The ERT technology has inherent limitations. And the spatial resolution of reconstructed images is fundamentally constrained by the number of electrodes and the inversion algorithm, which may fail to capture the finest details of hydrate morphology at the pore scale. However, it can observe changes in the distribution of hydrates at the macro scale. In this study, we employ a stable 16-electrode configuration and adopt the four-electrode measurement method for data acquisition. This approach separates current injection from voltage measurement, effectively eliminating the influence of contact impedance between electrodes and media, thereby obtaining measurement data with higher signal-to-noise ratio. Although it cannot directly improve the theoretical spatial resolution, the superior data quality provides a more reliable foundation for inversion algorithms, which helps us approach its resolution limit more closely under hardware limitations and reveal the macroscopic distribution of hydrates more clearly.

2.3. Electrical resistivity tomography apparatus

The self-developed ERT experimental system is mainly composed of an array electrode system that generates the excitation current, a data acquisition device and image reconstruction software (Lan et al., 2023). This device consists of five core modules, including pressure control system, temperature control system, ERT experimental instrument, data acquisition unit and image processing unit, which can not only capture and record the dynamic change of the electrical resistance during hydrate synthesis in real time, but also reconstruct the image of the sediments' resistivity at different moments (Fig. 2).

The pressure control system, also known as gas pressurization and output control system, is composed of a gas pressure reducing valve, a silent air compressor, a gas booster pump, a gas mass flow controller, gas storage cylinder. It mainly supplies the methane gas needed for hydrate synthesis. The temperature control system adopts the advanced low-temperature thermostatic water bath control program, and is particularly designed to integrate an external circulating pump. The temperature regulation range of the system covers from −20 to 90 °C with an accuracy of ±0.3 °C. It not only greatly improves the operation convenience, but also simplifies the use process. The ERT experimental cylinder is made of nylon material with MΩ level. 5 layers of ring electrodes are distributed in the axial direction of the ERT experimental cylinder, in which 16 electrodes are arranged for each layer with 22.5° intervals, each layer of the ring electrode array works independently (Fig. 3(a)). The specific parameters of the ERT experimental cylinder are shown in Table 1. The data acquisition unit incorporates an

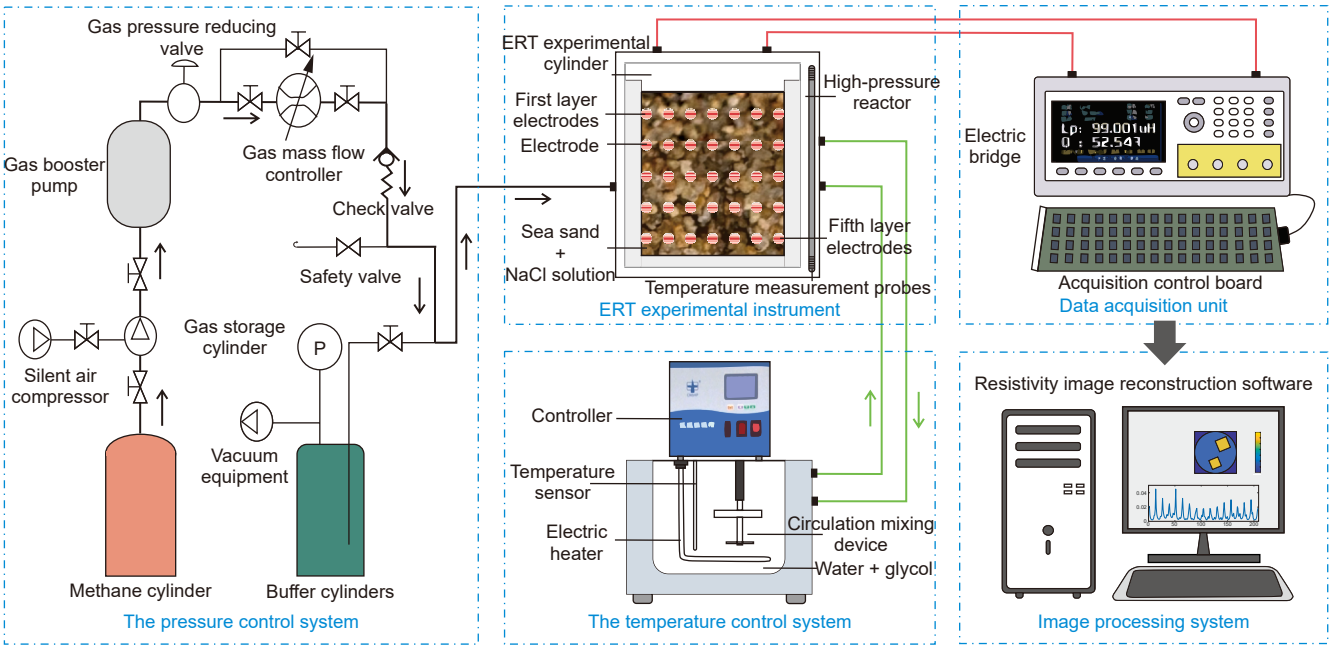


Fig. 2. Schematic diagram of hydrate ERT experimental setup.

Electric Bridge (Amber AT287A model) and an acquisition control board. The data acquisition is realized by using the adjacent excitation method (Fig. 3(b)). First, two neighboring electrodes are used as the power supply electrodes, and the potential difference between the remaining electrodes is measured sequentially. Second, the power supply electrodes are changed clockwise for the next set of measurements until 16 rounds of measurement cycles have been passed. Eventually, a total of 256 voltage values is measured during one acquisition (Seagar et al., 1987). The image processing unit is based on the self-developed NGH-E software to realize electrical resistance data processing and two-dimensional visualization of resistivity distribution, which adopts the Gauss-Newton iterative inversion technique. In our experiments, 5 sections can be obtained because there are 5 layers of ring electrodes.

2.4. Experiments of hydrate generation

The main purpose of this paper is to study the differences between sandy and muddy sediments in the synthesis of hydrates. In other words, this research aims to study the control of sediment inhomogeneity on the dynamic resistivity characteristics of marine hydrates. Typical sea sand and clayey silt sediments are selected for hydrate synthesis experiments. And the particle size distribution test and specific surface area analyses are carried out for the two sediments. The sea sand is characterized with high-purity quartz and coarse grains in which pore-filling hydrates are more easily generated, with the distribution ranging from 500 to 1800 μm, mainly concentrated around 800–1100 μm. Clayey silts, from silty seafloor sediments of the South China Sea, are rich in

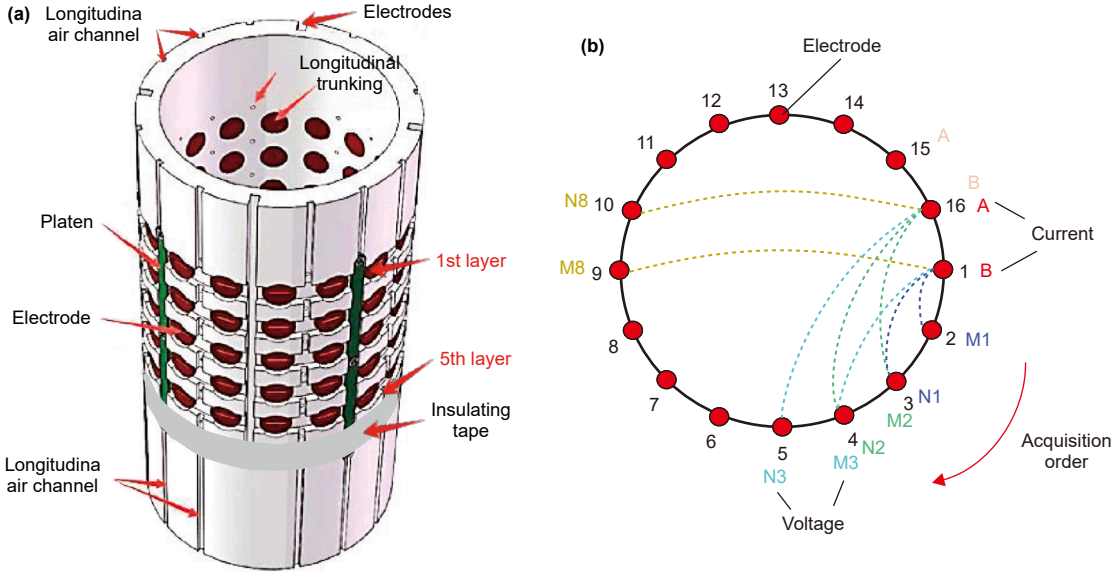


Fig. 3. The ERT experimental instrument. **(a)** Inner cylinder structure of ERT experimental instrument, **(b)** adjacent excitation data acquisition method.

Table 1
The parameters of ERT experimental cylinder.

Parameter	Total length, mm	Inner depth, mm	External diameter, mm	Inner diameter, mm	Diameter of electrode, mm	Layer spacing of electrodes, mm	Fifth layer of electrodes from the bottom, mm
Value	210	180	120	100	12	20	30

natural water and are characterized with fine-grained sediments, with an extremely wide range of particle size from 0.02 to 2000 μm, mainly concentrated in the range of 5–65 μm. And this type of fine-grained sediments is more likely to generate fracture-type hydrates (Chen et al., 2019) (Fig. 4). The adsorption isotherm data are analyzed using the BET method (multi-layer adsorption theory). Linear fitting yields the slope and intercept, enabling calculation of specific surface areas (Fig. 5). A striking contrast emerges: sea sand exhibits a specific surface area of just 0.79 m^2/g, whereas clayey silt sediments of the South China Sea demonstrate a substantially higher value of 13.90 m^2/g—exceeding the sea sand value by over 17 times.

To ensure the robustness and repeatability of the observed phenomena, three repeated hydrate formation experiments are conducted. The steps of a complete hydrate formation experiment are as follows: 1) For sea sand, a volume of 600 mL of sea sand calculated by the drainage method, is placed in the ERT experimental cylinder and compacted appropriately (Fig. 6). The porosity of sea sand is 38.88% according to volumetric method. To ensure uniform pore water distribution, a NaCl solution with a concentration of 3.5% (seawater salinity) is gradually injected into sediments until sediment is saturated with NaCl solution. For clayey silt, 600 mL of the South China Sea sediment (100% saturated with water) preserved in its original state in the laboratory is placed in the inner cylinder (Fig. 6). 2) The reactor is pressurized with methane. After the pressure stabilizes, the temperature of control system is set to 272.15 K to cool the reactor and initiate the formation of hydrates. 3) Maintaining the system temperature until the pressure inside the reactor is no longer decreases and stabilized for a prolonged period, indicating the substantial cessation of hydrate formation. Then the reactor is heated and depressurized, and a round of the experiment is completed. It should be noted that for hydrate formation experiments in sea sand sediments, the sediments are reused repeatedly. Before the next repeated experiment, the sediments must be carefully cleaned (desalinated) and dried. The experimental scheme is shown in Table 2.

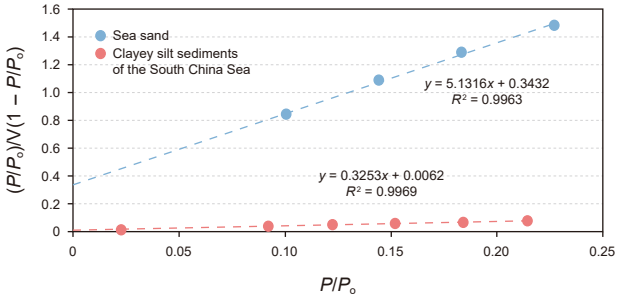


Fig. 5. The specific surface area is calculated using the multi-layer adsorption theory.

3. Results and discussion

3.1. Physical change in sediments

Pressure serves as the primary monitoring indicator for hydrate formation and dissociation. And the pressure variations arise from temperature drops and methane consumption during hydrate synthesis. Typically, an initial rapid pressure drop is caused by a decrease in temperature, followed by a gradual decline attributable to hydrate generation. The stabilization of pressure (i.e., the cessation of change) indicates that hydrate synthesis is nearly complete. Fig. 7 illustrates this pattern using experimental data from sea sand and clayey silt sediments of the South China Sea. According to the changes of pressure, the formation process of hydrates is divided into three stages. Following a 24-h stabilization period (Stage I) to ensure system airtightness and gas equilibrium, the reactor temperature is set to 272.15 K (Stage II). This triggers rapid cooling and pressure decrease, initiating hydrate synthesis. Subsequently (Stage III), with temperature stable, pressure declines slowly until stabilizing, indicating substantial hydrate synthesis has ceased.

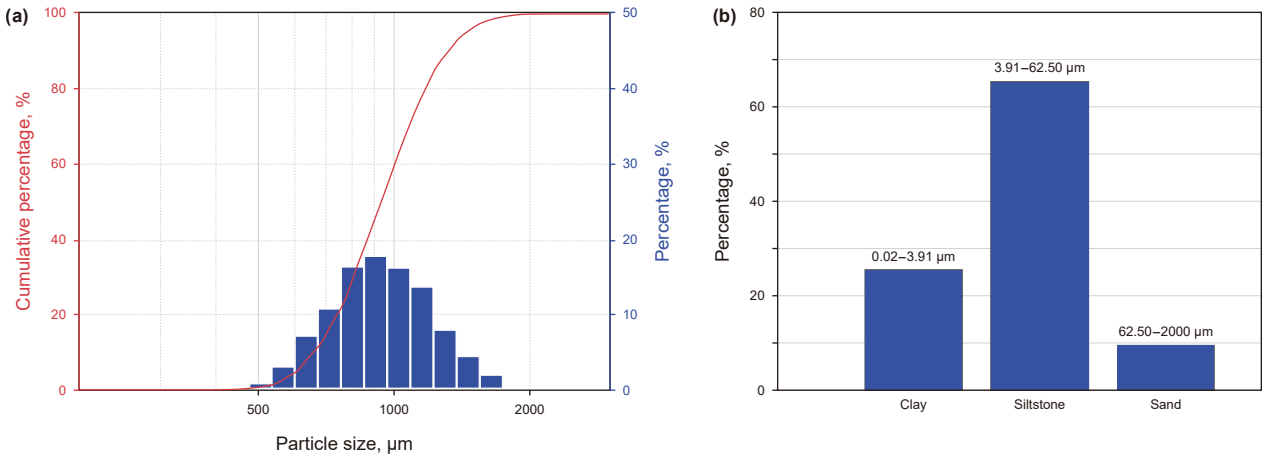


Fig. 4. Grain size of sediment samples. **(a)** Sea sand with the distribution ranging from 500 to 1800 μm, mainly concentrated around 800–1100 μm, **(b)** clayey silt sediments of the South China Sea with an extremely wide range of particle size from 0.02 to 2000 μm, mainly concentrated in the range of 5–65 μm (Su et al., 2021).

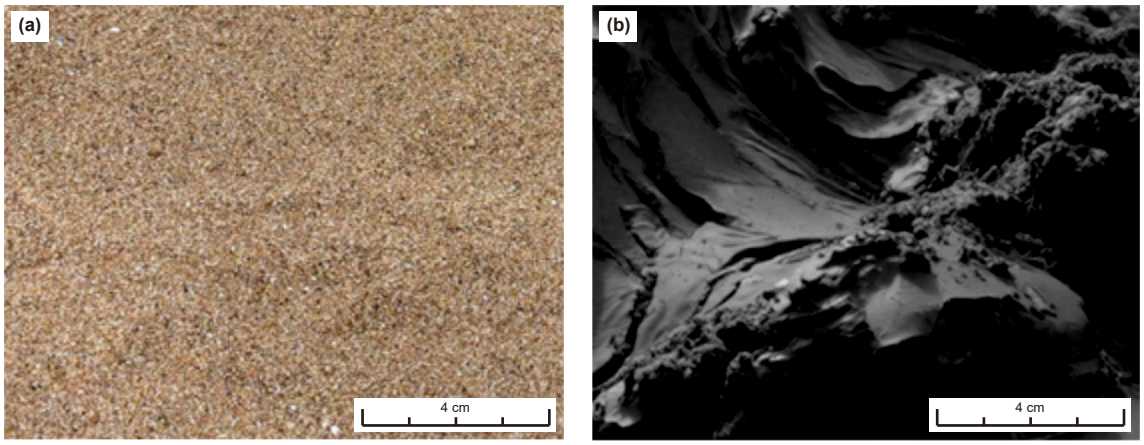


Fig. 6. Sediment. **(a)** Sea sand, **(b)** clayey silt sediments of the South China Sea.

Table 2
Experimental scheme for coarse and fine sediments.

Group	Kinds of sediments	Solution	Volume, mL	Porosity, %	Permeability, mD	Temperature of experiments, K
1	Sea sand	NaCl solution with a concentration of 3.5%	600	38.88	74	272.15
2	Clayey silt sediments of the South China Sea	Sea water	600	65.00	0.024	272.15

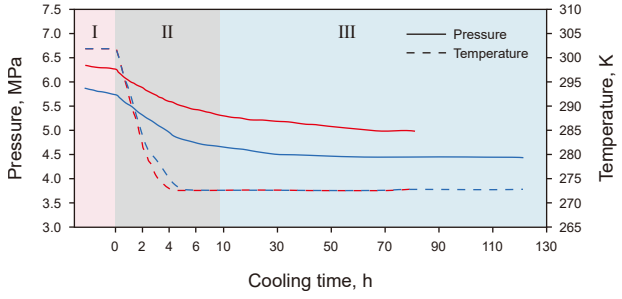


Fig. 7. A set of representative temperature and pressure curves recorded during the experiments. The blue line and red line represent sea sand and clayey silt sediments of the South China Sea, respectively. The initial pressure in the experimental design is set within a range of 5.5 to 6.5 MPa, resulting in different initial pressures for the two sediment experiments shown in the figure. However, this difference does not affect the characteristics of hydrate growth.

In both experiments, the reactor is opened at the end of hydrate synthesis to observe the hydrate distribution. The milky-white mass structures near the electrodes and scattered in the sea sand are hydrates synthesized in the experiment (Fig. 8(a) and (b)). These masses fill almost the entire pore space of the sediments and larger hydrate masses are formed in local areas. At the beginning of the experiment, the sediments placed in the reactor can be regarded as a uniformly distributed loose body, which makes it difficult to maintain a specific shape. However, after a series of complex physicochemical processes, such as pressurization, cooling and subsequent hydrate synthesis and decomposition, the originally soft sediments became unusually hard due to the cementation of hydrates and could be broken with the help of a small hammer (Fig. 8(b)). Hydrates synthesized in sea sand sediments fill and modify the original pore structure in solid form. When a piece of broken sediment is placed into the pre-prepared water, the surface of the water is quickly covered with dense bubbles. Gradually, the sediment begins to disintegrate, and eventually disperses into grains and grains of sea sand. As the hydrate continues to decompose, the amount of methane gas released increases dramatically, creating a small turbulent current underwater (Fig. 9).

It is difficult to directly observe the clumps of hydrates with the naked eye with fine-grained sediment, but the generation of hydrates makes the sediments hard (Fig. 8(c)). Most of the hydrates in fine-grained sediments in nature are distributed in fine pores and fractures. When water is injected into the cylinder, fine bubbles emerge continuously. These bubbles are a visual representation of the methane gas released from hydrate decomposition, which confirms the successful synthesis of hydrates (Fig. 8(d)). Visual inspection after reactor opening reveals that hydrate formation in both sediments exhibits significant spatial heterogeneity.

3.2. Resistivity changes of hydrate-bearing sediments

3.2.1. The resistivity changes with the growth of hydrates in the sea sand

A typical set of data from three repeated hydrate formation experiments is selected for presentation and analysis in this study. Fig. 10 visualizes the electrical resistance measures when the sediments are fully mixed with the 3.5% NaCl solution at room temperature and atmospheric pressure. The maximum value of the electrical resistance is stably distributed between 120 and 150 Ω, while the minimum value is close to 0.1 Ω. In addition, logarithmic conversion of the electrical resistance values is used to amplify the differences between the electrical resistance of the sediments. The electrical resistance of the sediments in each layer shows a small difference after logarithmic conversion, which proves the homogeneity of the internal structure of the sediments without hydrates.

After starting the experiment, the decrease in temperature causes a plunge in pressure. Initially, the pressure drops rapidly from 5.74 to 4.86 MPa in just 4.5 h, and then the decrease gradually

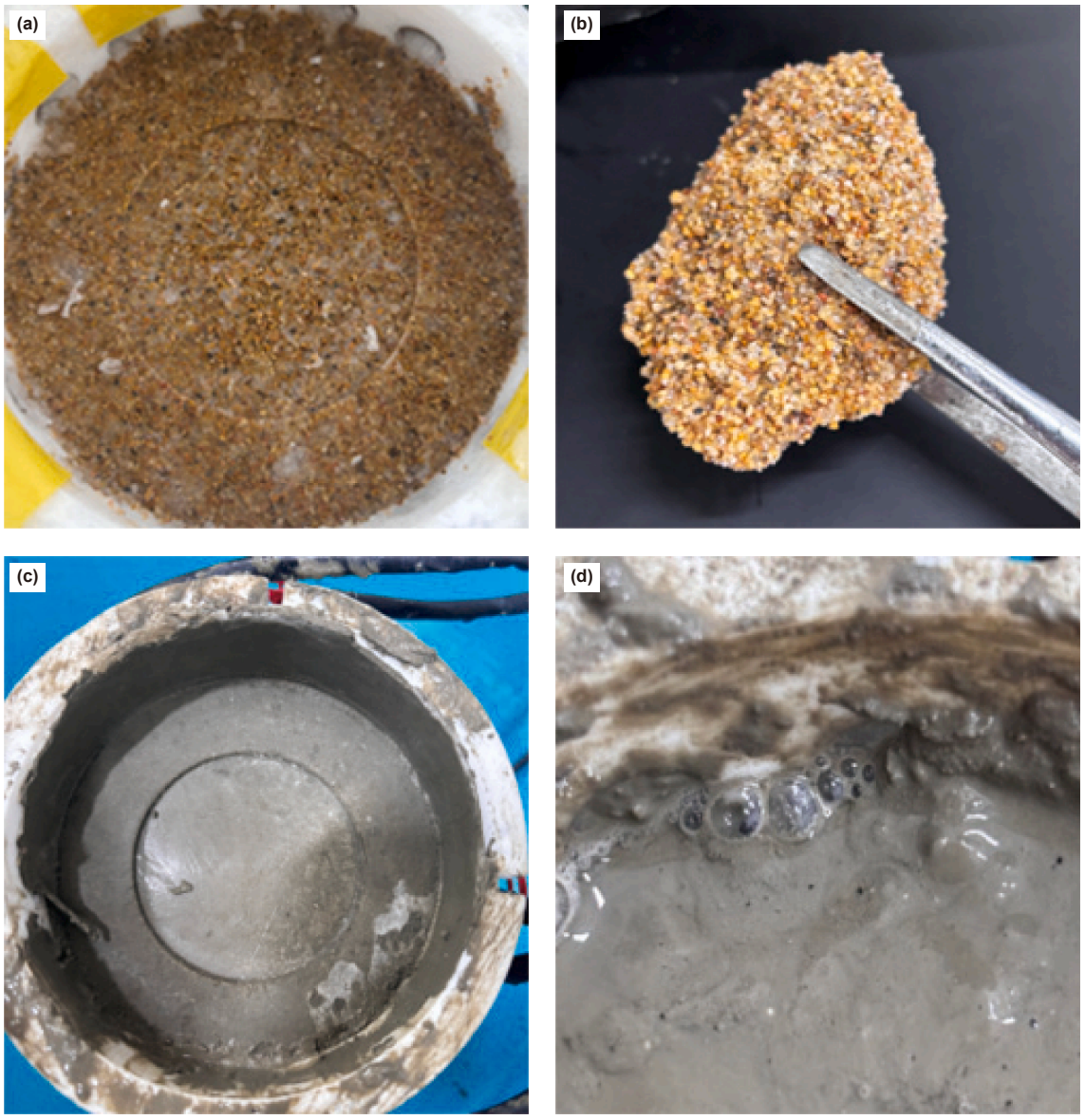


Fig. 8. Hydrate synthesis situation. **(a)** Hydrates distribution after synthesis based on sea sand, **(b)** broken hydrate-bearing sediments, **(c)** hydrates distribution after synthesis based on clayey silt sediments of the South China Sea, **(d)** bubbles from hydrate decomposition.

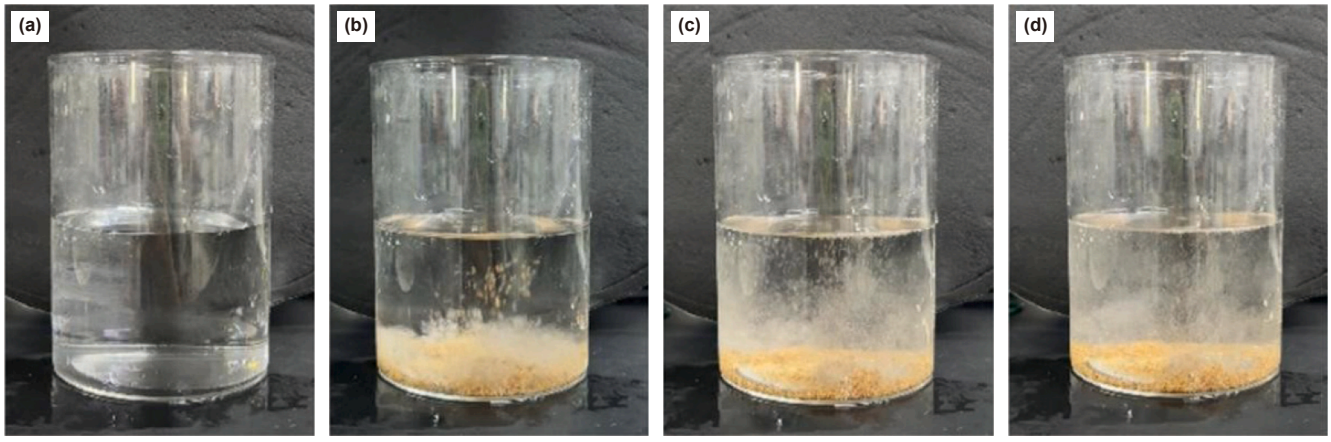


Fig. 9. Hydrate decomposition produces a large number of bubbles. And the presence of the bubbles makes the water cloudy.

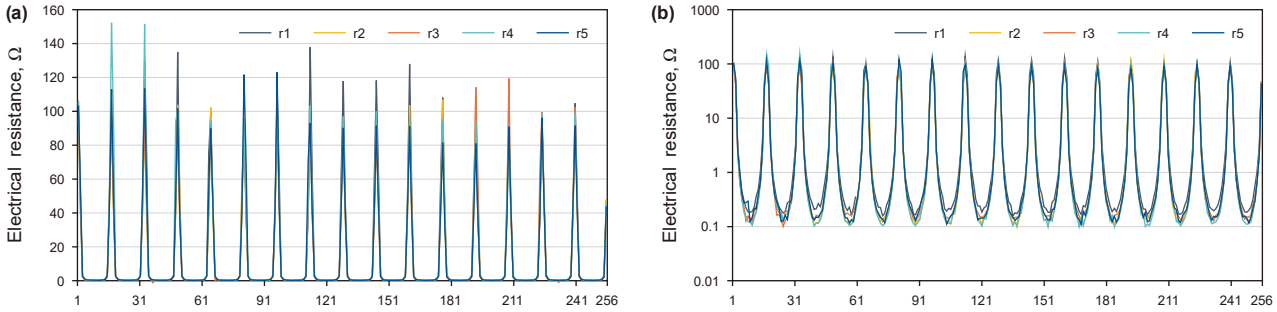


Fig. 10. Measurement results of sediment mixed with NaCl solution at room temperature and atmospheric pressure. **(a)** Actual measured electrical resistance data, **(b)** results after taking logarithm of electrical resistance data. Where r1–r5 represent the 1st to the 5th layer of the ERT inner cylinder, respectively.

slows down until it reaches a stable level of 4.46 MPa. The phenomenon shows that the electrical resistance of the upper layer increased rapidly, and the lower region increased slowly. And with the increase of time, the upper region change gradually becomes slower, the difference between the upper and bottom regions of the smaller. In order to facilitate the description of the changes in reservoir resistivity during the formation of hydrates, we selected representative moments in several stages of hydrate formation to elaborate, including the end of rapid cooling, the period of active growth and the point of pressure stabilization. At 5.5 h of experimentation, the maximum value of the bottom region is close to 300 Ω, while the upper region averaged at 400 Ω, and the maximum value of electrical resistance has already reached close to 600 Ω. The upper region is significantly higher than the bottom in terms of minimum value with electrical resistance (Fig. 11(a)). When the experiment has been going on for 10.5 h, it shows electrical resistance peaks reaching 600 Ω, with the lower "U"-zone values rising to 1 Ω. According to the vertical electrical resistance disparity (upper vs. bottom), hydrate growth is heterogeneous (Fig. 11(b)). This phenomenon is mainly due to the fact that the upper region of the reactor is in direct contact with the methane gas, and hydrate is preferentially generated at the gas-water contact surface. Subsequently, the electrical resistance begins to grow slowly, suggesting that hydrates are also gradually being generated, particularly in bottom reactor regions, as evidenced in Fig. 11(c). When the experiment has been going on for 107 h, peak electrical resistance approaches 800 Ω, with logarithmic transformation revealing multi-uniform "U" distribution indicating a relatively balanced hydrate synthesis in each layer. And even the lower electrical resistance is kept above 1 Ω, which shows the remarkable and uniformity of the overall hydrate synthesis. When the pressure change almost stops, indicating that the hydrate synthesis is no longer continuing, stop the round of experiments.

In exploring the spatial distribution characteristics of the hydrate synthesis process, it is illustrated both horizontally and vertically. It means that resistivity images of the same layer at different moments and of different layers at the same moment are selected for comparative analysis, which reveals non-uniformity in hydrate synthesis. Fig. 12 shows the evolution of the resistivity distribution within the sediments at the beginning of hydrate synthesis is selected for illustration. Initially, the system shows homogeneous resistivity (average 1.52 Ω·m) after pressurization without cooling. At $t = 1.5$ h after the initiation of cooling, localized resistivity increases to 5.2 Ω·m with an average rise to 2.48 Ω·m (Fig. 12(b)). After 5.5 h of cooling, electrode-adjacent regions exhibited significantly higher resistivity than central areas (Fig. 12(c)), indicating that the synthesis of hydrate has an obvious positional preference. Hydrates can be generated rapidly in a certain location because there is good gas-water contact there, and this phenomenon is consistent with Sloan Jr and Koh (2007).

Fig. 13 compares resistivity distributions across reactor layers after 10.5 h of cooling. Upper layers (closer to methane source) show higher average resistivity (7.08 Ω·m in the first layer vs. 4.16 Ω·m and 3.85 Ω·m in the third/fifth layers). This phenomenon can be attributed to the direct contact between the upper layer of the ERT inner cylinder and methane gas, which provides abundant gas conditions for hydrate synthesis, thus accelerating the hydrate formation process in this region. Hydrate generation hinders the top-down transport of methane, making upper regions hydrate hotspots with significantly greater formation intensity than bottom areas. This spatial contrast confirms proximity to gas source enhances synthesis efficiency. Meanwhile, we can conclude that the influence of the gas source is also one of the important reasons for the heterogeneous generation of hydrates. After 107 h of cooling, the average resistivities of the electrodes in the first, third and fifth layers are stable at 7.43, 6.21 and 5.78 Ω·m, respectively. This convergence of resistivity values indicates that initially slow-forming regions are now actively synthesizing hydrates, resulting in diminished vertical disparities between layers. Eventually, the spatial distribution of hydrate generation becomes progressively balanced during late synthesis (Fig. 13). Notably, the third and fifth layers exhibit higher resistivity in central regions than near electrodes. It can be speculated that hydrates in the bottom part of the reactor preferentially form in the center of the deposit. This inversion may result from upper-layer hydrate growth in the electrode location obstructing current conduction channels, impeding methane migration downward. Consequently, the central sediment retains more intact gas pathways, sustaining upper-to-bottom methane transport.

3.2.2. The resistivity changes with the growth of hydrates in the clayey silt sediments

At the beginning of the experiment in the clayey silt sediments of the South China Sea, the maximum value of the electrical resistance is mainly concentrated in the range of 60~80 Ω, while the minimum value is as low as below 0.1 Ω, when the pressure is 6.34 MPa (Fig. 14(a)). While hydrate experiments conducted with sea sand show maximum electrical resistance values ranging from 120 to 160 Ω under similar temperature and pressure conditions, the electrical resistance measured in the clayey silt sediments of the South China Sea experiments is markedly lower. The additional conductive effect caused by the double electric layer of muddy sediments is the main reason (Saidian et al., 2016).

After remaining stationary for 24 h, the pressure system values stabilize and remain unchanged. Then, the constant temperature system is activated to start the experiment. Only 6 h after the cooling operation is carried out, the pressure drops dramatically to

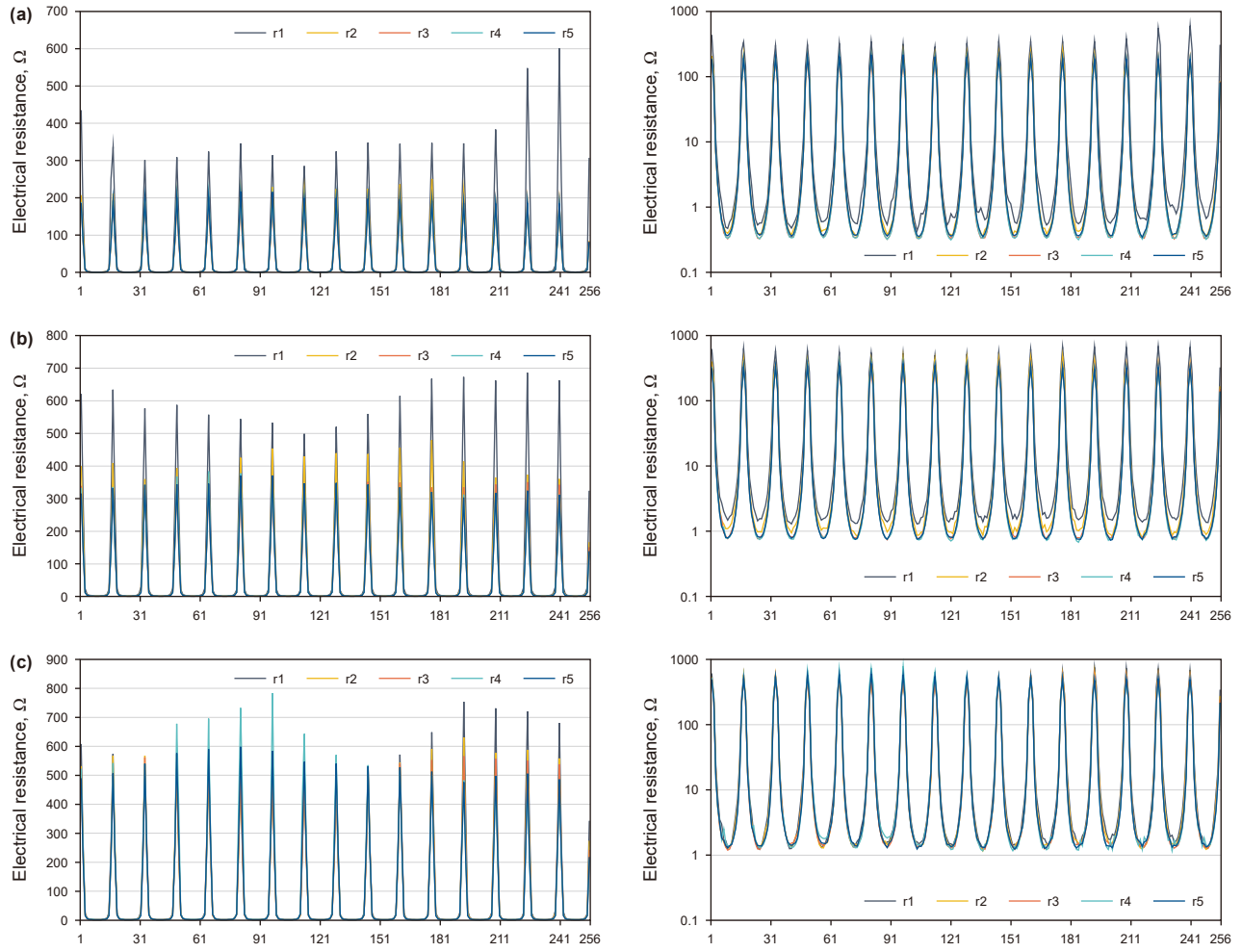


Fig. 11. Measurement results during hydrate synthesis with sea sand. **(a)** Electrical resistance data measured at $t = 5.5$ h after cooling. **(b)** Electrical resistance data measured at $t = 10.5$ h after cooling. **(c)** Electrical resistance data measured at $t = 107$ h after cooling. Where r1–r5 represent the 1st to the 5th layer of the ERT inner cylinder.

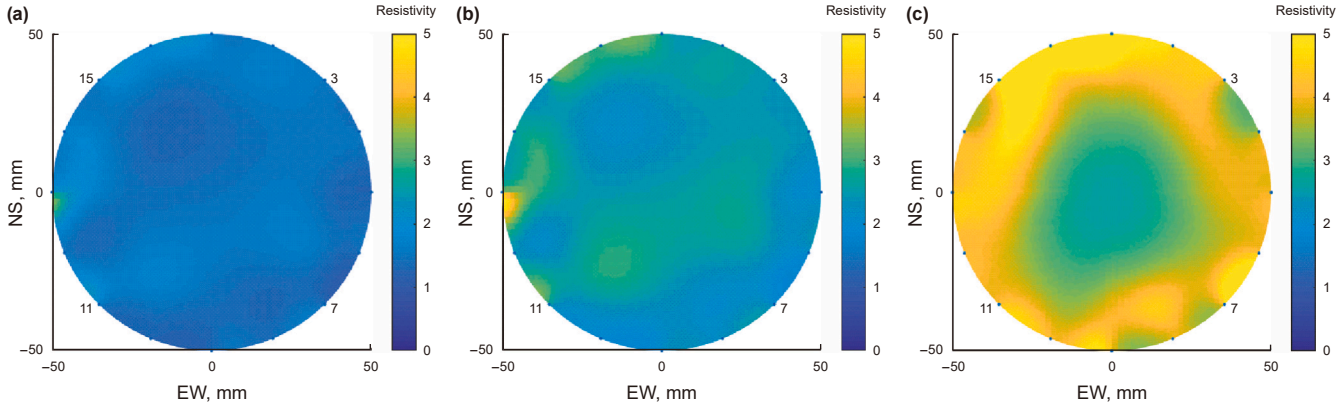


Fig. 12. Resistivity image at the beginning of hydrate synthesis. **(a)** Resistivity image in the reactor after pressurization without cooling, **(b)** resistivity image in the reactor at $t = 1.5$ h after cooling initiation, **(c)** resistivity image in the reactor at $t = 5.5$ h after cooling initiation.

5.40 MPa. It's mainly caused by a drop in temperature. The electrical resistance changed drastically as shown in Fig. 14(b), with the maximum value soaring to 900 Ω. Even in logarithmic coordinates, the originally small electrical resistance at the bottom of the U-shape increased to about 1 Ω. Meanwhile, the electrical resistance data recorded in bottom region is more prominent than that recorded in the upper region. At this point, hydrate begins to synthesize, and the change in electrical resistance is mainly due to a combination of the decrease in temperature and hydrate formation.

Further, the electrical resistance continues to grow significantly, and the maximum value of the electrical resistance is close

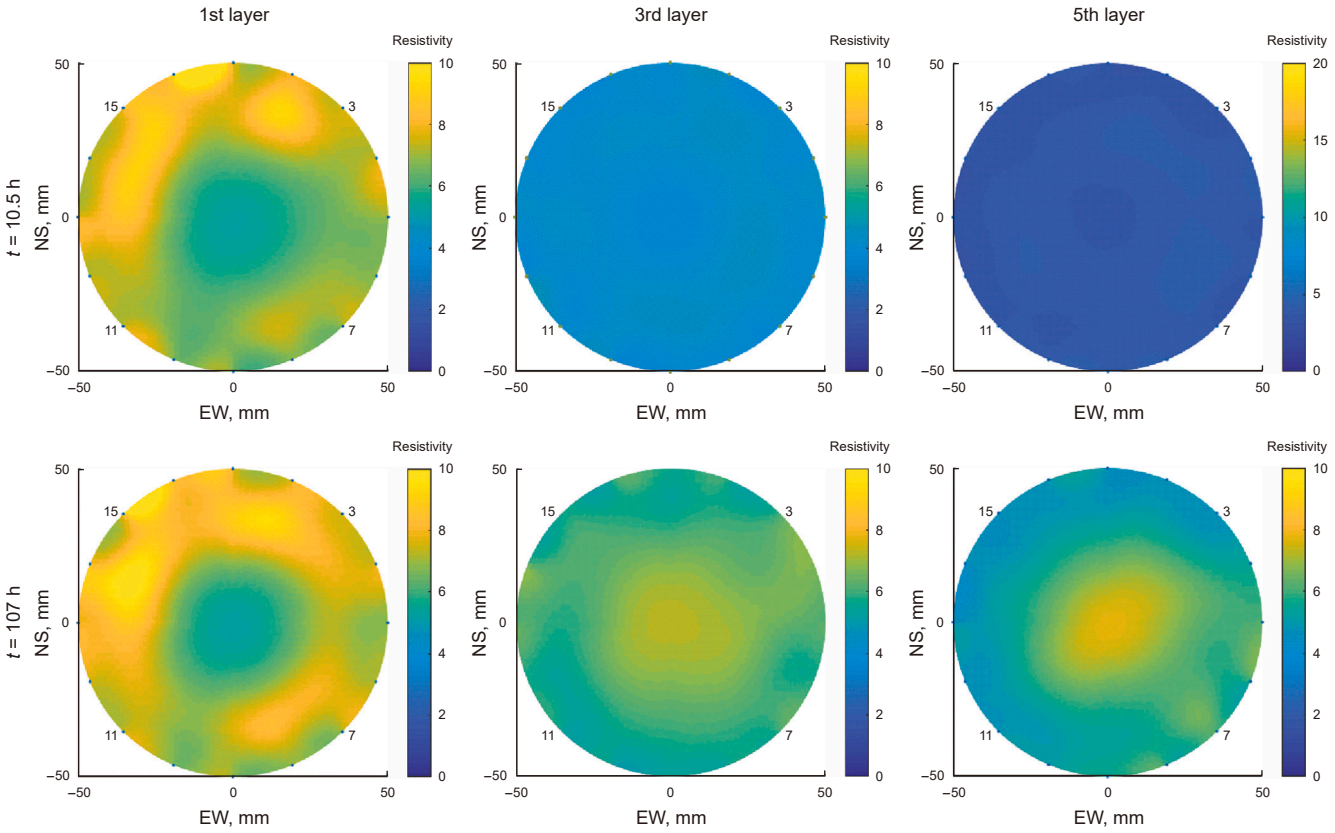


Fig. 13. Resistivity images of different layers and different moments with sea sand.

to 4000 Ω after the cooling process has lasted for 53 h, while the minimum value of the electrical resistance in the rest of the area is more than 10 Ω except for the upper region, which clearly indicates the beginning of hydrate synthesis in large quantities. At this time, the difference between the electrical resistance of the upper and bottom positions in the reactor is significantly enlarged (shown in Fig. 14(c)).

The above resistance data are subsequently inverted to capture the resistivity distribution in the reactor at the same moment in time. The upper and bottom layers are chosen as examples (Fig. 15). Due to the double electric layer effect, the resistivity of clayey silt sediment is lower than the sea sand. Anomalously high values of localized resistivity appeared in the bottom region image after the reactor is pressurized, and this anomaly is hypothesized to be the presence of methane gas. Within a short period of time, the average resistivity of the upper region increases from the initial 0.58 to 4.14 Ω·m. However, the resistivity in bottom region changes even more drastically from 0.78 to 8.87 Ω·m, which is more than a tenfold increase.

After 53 h cooling, a substantial increase in the average resistivity is observed which grows to 34.38 and 90.73 Ω·m, respectively. It is believed that a large amount of hydrate synthesis. Compared to the environment of sea sand (Figs. 12 and 13), hydrates tend to form in the center region of the reactor, and synthesis is far more effective than expected. The fine-grained sediments have a larger specific surface area (Fig. 5), which increases the contact area between methane and water molecules and facilitates hydrate nucleation. Although the original pore connectivity is poor in fine-grained sediments, it may show a double effect under high-pressure conditions (Hu et al., 2024). Meanwhile, the clayey silt sediments are prone to form fractures. CT imaging prior to cooling (pre-hydrate synthesis) reveals abundant fine, interconnected micro-fractures within pressurized clayey silt. At the field, this type of fine-grained sediments is also the exact areas where fractures develop (Riedel et al., 2006; Li et al., 2012). These fractures provide crucial channels for methane transport and space for hydrate synthesis, explaining why the bottom region of the reactor becomes favorable for hydrate formation (Fig. 16). Furthermore, reconstructed images from hydrate synthesis experiments based on clayey silt sediments of the South China Sea reveal localized high-resistivity zones in the bottom and central regions. These high-resistivity signals directly indicate substantial hydrate synthesis, and the spatial distribution of these zones corresponds fundamentally to areas of dense fracture development observed in initial CT scans.

3.2.3. *Comparison of resistivity between field data and experimental results*

Well logging data from the Shenhu area are collected. The in-situ resistivity values generally fall within the range of 1 to 7 Ω·m (Wang et al., 2014; Zhan et al., 2022; Wei et al., 2018; Zhang et al., 2017). These values are considerably lower than the resistivity levels observed in our experimental samples. To further contextualize these findings, we examined well logging data from the Qiongdongnan Basin and Taixinan Basin of the South China Sea, which reveal a remarkably wide range of resistivity from a few to several thousand ohms per meter (Wang et al., 2017; Liang et al., 2019). In this context, the resistivity increase observed in our experiments from several to several tens of ohms per meter in hydrate-bearing clayey silt appears consistent with the natural settings. As illustrated in Fig. 16, the pressurized clayey silt samples contain numerous fine, interconnected micro-fractures. The formation of hydrates within these fractures creates a highly

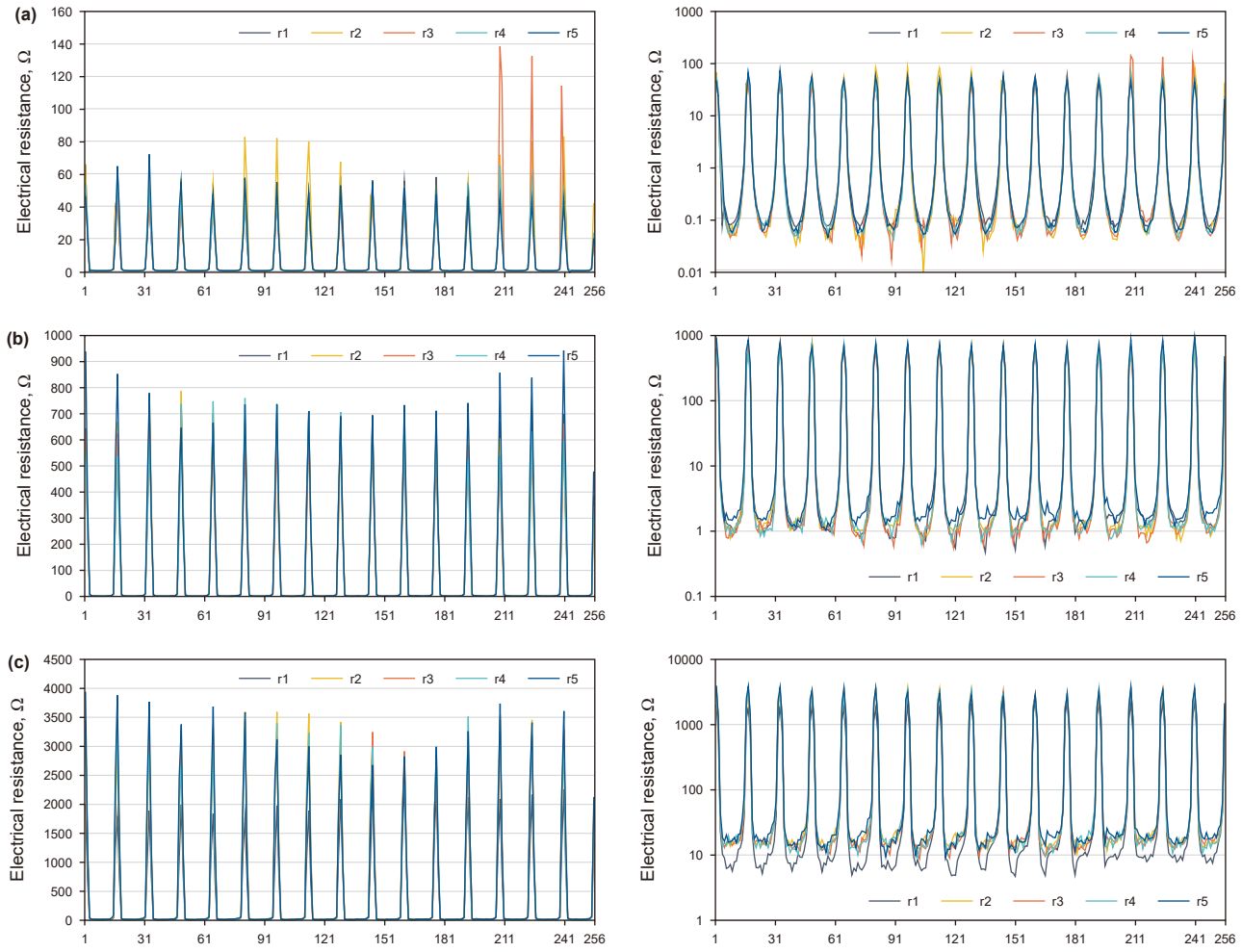


Fig. 14. Measurement results during hydrate synthesis with clayed silt seafloor sediments of the South China Sea. **(a)** Electrical resistance data measured after pressurization without cooling, **(b)** electrical resistance data measured at $t = 6$ h after cooling, **(c)** electrical resistance data measured at $t = 53$ h after cooling. Where r1–r5 represent the 1st to the 5th layer of the ERT inner cylinder.

resistive skeleton, which explains the elevated resistivity values of several tens of ohms per meter measured in our experiments.

When we compare the resistivity of two sediments, we will find that the clayey silt achieved a maximum average resistivity of 90.73 Ω·m in its most productive layer, which is an order of magnitude higher than the 7.43 Ω·m measured in the most productive layer of the sea sand (Figs. 13 and 15). However, we observe that the pressure decline between these two sets of experiments shows little difference, indicating that the saturation of hydrates in the entire sedimentary system is close. Although fracture-developed reservoirs can exhibit higher resistivity even at relatively low hydrate saturations (Heeschen et al., 2016; Xu et al., 2022). This phenomenon is also observed in this study, when the saturation of hydrates is similar, the resistivity of clayey silt sediments with developed fractures is much higher than that of sea sand sediments. Therefore, in clay-rich sedimentary systems with fractures, the resistivity signature is a complex product of hydrate saturation, spatial distribution and fracture connectivity. In quantitative evaluation of fracture-developed hydrate reservoirs, accurate selection of interpretation models is essential to avoid overestimation of hydrate saturation. In the ERT images of sea sand, resistivity anomalies typically appear as localized, well-defined, high-contrast patches. This pattern aligns with the concept of pore-filling hydrates occupying relatively homogeneous and well-connected pore spaces. In the ERT images of clayey silt, resistivity anomalies generally manifest as more diffuse, interconnected network-like patterns. It is noteworthy that due to the inherent resolution limitations of ERT, distinguishing between these patterns based on field ERT data remains highly challenging.

3.3. The impact of sediment heterogeneity on the hydrate growth

In the analysis of the previous section, it is known that there is a significant difference between sea sand and clayey silt seafloor sediments from the South China Sea in the hydrate synthesis process. And the amount of resistivity is positively correlated with hydrate saturation to a certain extent (Archie, 1942). It is worth emphasizing that the principal contribution of this 2D resistivity monitoring approach lies in its ability to visualize the spatial heterogeneity and temporal dynamics of the hydrate formation process, rather than providing a quantitative calibration for saturation inversion. Therefore, the resistivity profiles presented here are interpreted primarily in a qualitative and semi-quantitative manner. The type of sediment has a significant effect on the distribution and formation pattern during hydrate synthesis. Hydrates synthesized based on these two types of sediments can be approximated as pore-type and fracture-type hydrates,

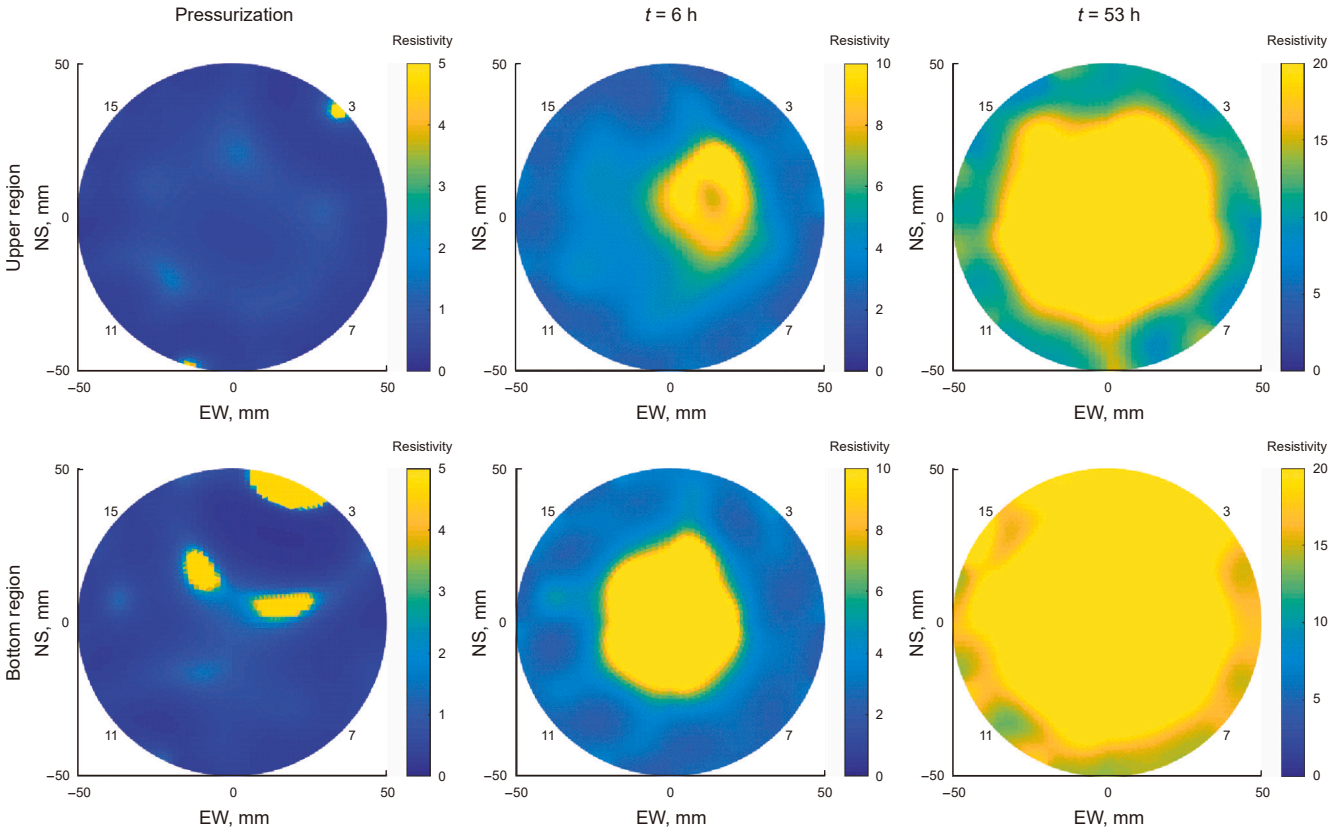


Fig. 15. Resistivity images of hydrate synthesis processes based on clayey silt seafloor sediments of the South China Sea.

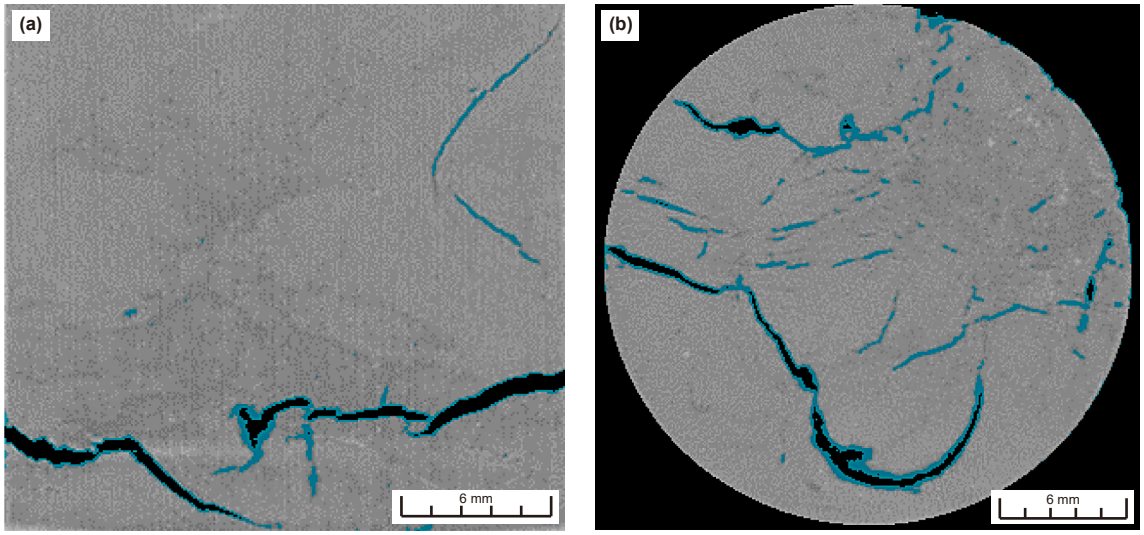


Fig. 16. Local CT images of clayey silt seafloor sediments of the South China Sea before hydrate synthesis. Where the black part is free gas and the blue part is NaCl solution.

respectively (Chen et al., 2019). Based on the sediments in the reactor, we constructed the distribution patterns of gas and water in the sediments, which is used to present the distribution and formation pattern during hydrate synthesis (Fig. 17). Shades of blue represent changes in water saturation. The areas of high water saturation tend to be accompanied by less methane gas, and some of the methane in these areas will dissolve in the water to form a methane solution.

In pressurized sea sand, the bottom of reactor is filled with the NaCl solution, resulting in a lower resistivity compared to the upper region. Even though the pores in the sea sand are relatively large and interconnected compared to those in clayey silt sediments of the South China Sea, allowing gas diffusion, the water makes it difficult for gas to enter the pore water at the bottom. Hydrate forms predominantly in upper pores, yielding poor synthesis efficiency in the water-saturated bottom region. In addition,

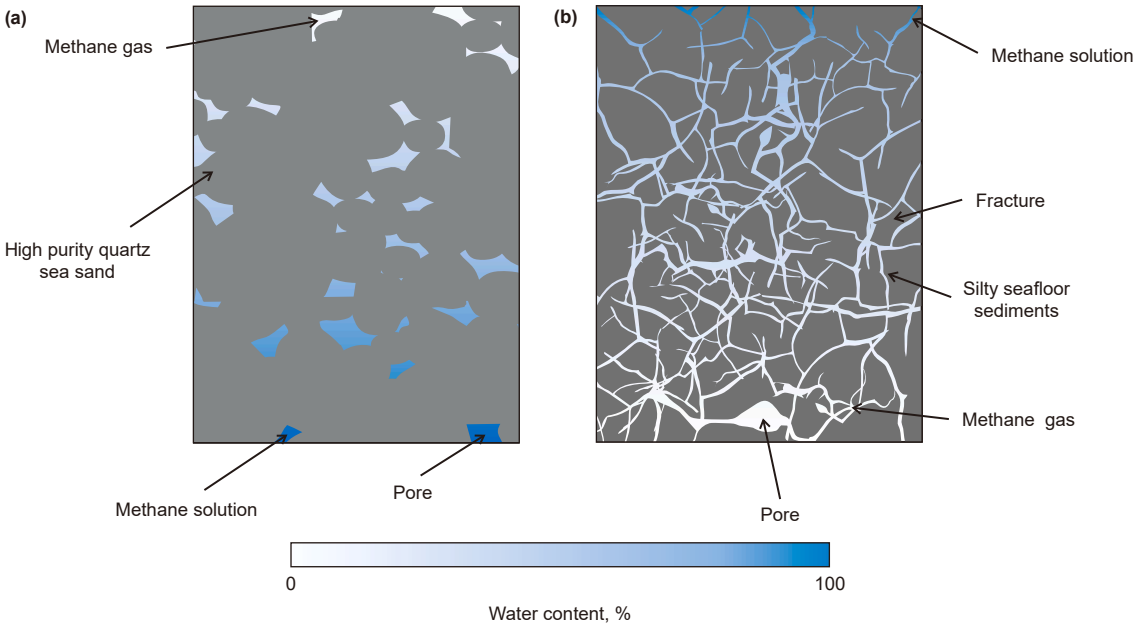


Fig. 17. Distribution patterns of gas and water in sediments. **(a)** Sea sand, **(b)** clayey silt seafloor sediments of the South China Sea.

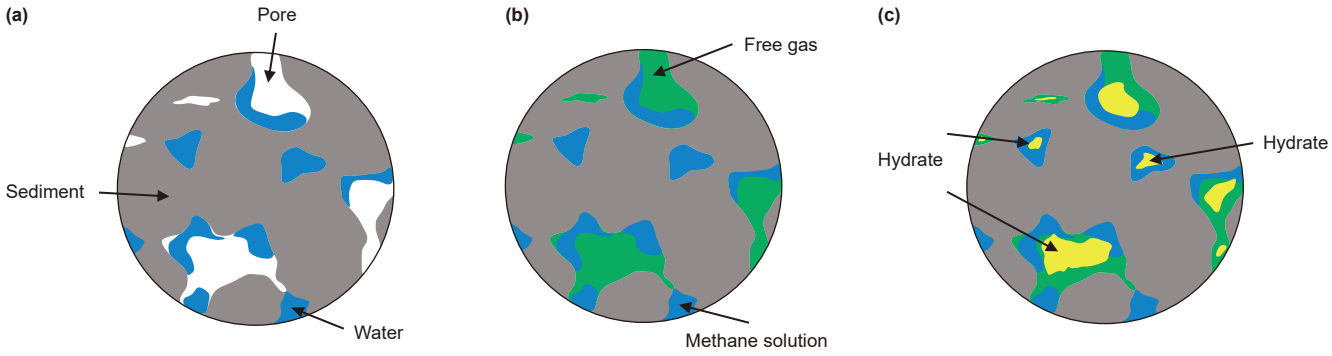


Fig. 18. The evolutionary mechanism of the hydrate generation process.

previous studies have also shown that the high water saturation of the sediment itself further weakens the overall hydrate synthesis (Johnson et al., 2022). In contrast, clayey silt sediments of the South China Sea exhibit fundamentally different behavior. In the upper of clayey silt sediments, the gas can't enter the micropores. Gas injection and sediment properties promote fracture development. These fractures serve as natural conduits, significantly enhancing the connectivity of internal pores in sediments, allowing methane gas to migrate smoothly to the bottom area of the reactor (Chen et al., 2022). Furthermore, clayey silt sediments of the South China Sea have a large specific surface area and abundant organic matter, which can promote hydrate nucleation (Kelleher et al., 2007). High upper-region water saturation impedes hydrate generation in clayey silt sediments of the South China Sea. Conversely, the bottom region benefits from fracture networks providing effective methane migration pathways and growth space. Therefore, hydrate synthesis is significantly more effective in the bottom region, which is observed in our experiments. If the gas is continuously supplied, the hydrate will accumulate in large quantities and be widely distributed in the areas with dense fractures, showing a more concentrated and continuous distribution pattern. We can conclude that the differences of pore structure, mineral composition, and organic matter content between sandstone and mudstone affect the hydrate synthesis.

The evolutionary mechanism of the hydrate generation process is described on the basis of the experimental results, see Fig. 18. Initially, when methane gas is injected into the interior of the core, the methane molecules are gradually incorporated into the solution in the pores through dissolution and diffusion. The sediment pores contain both free methane gas and dissolved methane gas. Methane exhibits a certain low solubility in water (Wiesenburg and Guinasso Jr, 1979; McGinnis et al., 2006; Zhao et al., 2022). Over time, methane gradually diffuses downward through the sediment in the form of dissolved gas. This process is not instantaneous but exhibits a dynamic characteristic of being initially fast and then slowing down, and it is time-consuming. Consequently, a methane concentration gradient develops within the sedimentary system. Once the pressure and temperature in the reactor reach the conditions for hydrate formation, hydrates preferentially nucleate in regions where the methane concentration first meets the nucleation requirements. As hydrate formation proceeds, the local methane concentration in the pore water of these regions decreases, thereby enhancing the local concentration gradient and driving continuous methane dissolution and replenishment of

reactants (Li et al., 2012; Lei et al., 2019). In other word, the hydrate formation shows a selective growth pattern. Hydrate formation starts preferentially in pore areas with high methane concentrations, which are “hot spots” for hydrate formation due to the abundant supply of methane gas. Subsequently, as methane is further dissolved in water, hydrates are gradually formed in these solutions. The concentration of methane determines the amount of hydrate synthesized.

For sea sand, our experimental results are consistent with previous studies, with the ERT images similarly demonstrating the phenomenon of localized enrichment (Priegnitz et al., 2013). Unfortunately, no laboratory studies have yet been conducted on clayey silt. And in field settings, the observed pore-filling hydrates in sandy reservoirs and fracture-filling hydrates in clayey silt reservoirs correspond precisely to the two hydrate types simulated in our study (Jia et al., 2016; Makogon, 2010). Compared to pore-filling hydrates, fracture-filling hydrates are controlled by fracture development, exhibit strong spatial heterogeneity, and tend to locally generate high-saturation hydrate accumulations (Cook et al., 2014; Boswell et al., 2012). Furthermore, in fracture-filling hydrate reservoirs, the hydrate quantity within specific zones can be substantial, yet the average saturation remains low with high heterogeneity, posing significant challenges for accurate reserve assessment (Jin et al., 2025; Lee et al., 2013). While fractures provide initial pathways, the low-permeability matrix impedes heat transfer and water removal. This limitation may lead to pore blockage by ice or secondary hydrates (Zhao et al., 2022; Yin et al., 2016). Therefore, the decomposition of high-saturation hydrates in these localized zones also carries greater risks, such as formation collapse and engineering incidents. In contrast, pore-filling hydrates in sea sand are considered primary targets for production because the connected pore space facilitates fluid flow (gas and water) during decomposition, resulting in higher safety and controllability. Consequently, most existing hydrate production trials have been conducted in sandy reservoirs (Fujii et al., 2013; Zhao et al., 2022).

4. Conclusion

Based on hydrate electrical synthesis experiments utilizing the ERT system, this study investigated the variations in pressure and electrical resistance, employing the Gauss-Newton iterative method to transform these data into visualized images. This approach elucidated the dynamic processes underlying hydrate formation. The principal findings are summarized as follows:

(1) Distinct vertical resistivity patterns emerge during hydrate synthesis in sea sand and clayey silt sediments of the South China Sea. In sea sand, resistivity progressively decreases from upper (7.43 Ω·m) to bottom (5.78 Ω·m) within >100 h, indicating preferential hydrate formation in shallower regions. Conversely, clayey silt exhibits inverse behavior: resistivity increases from upper (34.38 Ω·m) to bottom (90.73 Ω·m) after >50 h, revealing significantly enhanced hydrate formation in deeper zones. Comparatively, the clayey silt sediments of the South China Sea achieve higher and more efficient hydrate synthesis.

(2) Sediment heterogeneity governs hydrate distribution and resistivity evolution by controlling gas-water behavior and pore structure. In sea sand, pores water restricted methane diffusion, which results in hydrate formation near the gas source. Conversely, abundant fractures in mud sediments enhances methane transport, enabling widespread and concentrated hydrate growth in fractured zones. Furthermore, hydrate formation exhibits inherent selectivity, preferentially occurring in methane-rich regions while being impeded in water-saturated areas. Sediment properties dictate gas-water distribution and pore structure, which collectively determine hydrate formation patterns.

CRediT authorship contribution statement

Xi-Xi Lan: Writing – review & editing, Writing – original draft, Visualization, Validation, Data curation. **Qing-Tao Bu:** Methodology, Funding acquisition, Conceptualization. **Xiao-Li Hong:** Project administration. **Jin-Huan Zhao:** Validation, Supervision, Funding acquisition, Formal analysis. **Qiang Chen:** Resources, Project administration, Funding acquisition. **Yuan-Yuan Zhang:** Methodology, Formal analysis, Data curation. **Chang-Chun Zou:** Supervision, Project administration, Funding acquisition, Conceptualization. **Guang-Bo Xu:** Supervision, Software, Project administration, Methodology.

Declaration of competing interest

The authors declare the following financial interests/personal relationships which may be considered as potential competing interests: Jinhuan Zhao reports financial support was provided by the National Natural Science Foundation of China (Grant No. 42206232). If there are other authors, they declare that they have no known competing financial interests or personal relationships that could have appeared to influence the work reported in this paper.

Acknowledgments

This work is supported by the National Natural Science Foundation of China (No. 42206232, No. 42274232, No. 42376218, No. 42376067), the Natural Science Foundation of Shandong Province of China (ZR2024MD083), and also funded by Marine Geological Survey Program (DD20230064).

References

Adebayo, A.R., Kandil, M.E., Okasha, T.M., et al., 2017. Measurements of electrical resistivity, NMR pore size and distribution, and X-ray CT-scan for performance evaluation of CO_2 injection in carbonate rocks: a pilot study. Int. J. Greenh. Gas Control 63, 1–11. https://doi.org/10.1016/j.ijggc.2017.04.016.

Archie, G.E., 1942. The electrical resistivity log as an aid in determining some reservoir characteristics. Trans. AIME 146 (1), 54–62. https://doi.org/10.2118/942054-G.

Atig, D., Broseta, D., Pereira, J.M., et al., 2020. Contactless probing of polycrystalline methane hydrate at pore scale suggests weaker tensile properties than thought. Nat. Commun. 11 (1), 3379. https://doi.org/10.1038/s41467-020-16628-4.

Balasco, M., Lapenna, V., Rizzo, E., et al., 2022. Deep electrical resistivity tomography for geophysical investigations: the state of the art and future directions. Geosciences 12 (12), 438. https://doi.org/10.3390/geosciences12120438.

Bergmann, P., Schmidt-Hattenberger, C., Labitzke, T., et al., 2017. Fluid injection monitoring using electrical resistivity tomography—five years of CO_2 injection at Ketzin, Germany. Geophys. Prospect. 65 (3), 859–875. https://doi.org/10.1111/1365-2478.12426.

Bosch, D., Ledo, J., Queralt, P., et al., 2016. Core-scale electrical resistivity tomography (ERT) monitoring of CO_2–brine mixture in Fontainebleau sandstone. J. Appl. Geophys. 130, 23–36. https://doi.org/10.1016/j.jappgeo.2016.03.039.

Boswell, R., Collett, T.S., Frye, M., 2012. Subsurface gas hydrates in the northern Gulf of Mexico: fracture-controlled occurrence and resource implications. Mar. Petrol. Geol. 34 (1), 150–168. https://doi.org/10.1016/j.marpetgeo.2011.10.003.

Boswell, R., Hancock, S., Yamamoto, K., et al., 2020. Natural gas hydrates: status of potential as an energy resource. Fut. Energy 111–131. https://doi.org/10.1016/B978-0-08-102886-5.00006-2.

Chen, G., Li, C., Liu, C., et al., 2019. Effect of microscopic distribution of methane hydrate on resistivity in porous media. Adv. New Renewab Energy 7 (6), 493–499. https://doi.org/10.3969/j.issn.2095-560X.2019.06.004.

Chen, Q., Wu, N., Liu, C., et al., 2022. Research progress on global marine gas hydrate resistivity logging and electrical property experiments. J. Mar. Sci. Eng. 10 (5), 645. https://doi.org/10.3390/jmse10050645.
Cook, A.E., Goldberg, D., Malinverno, A., 2014. Natural gas hydrates occupying fractures: a focus on non-vent sites on the Indian continental margin and the northern Gulf of Mexico. Mar. Petrol. Geol. 58, 278–291. https://doi.org/10.1016/j.marpetgeo.2014.04.013.
Daily, W., Ramirez, A., LaBrecque, D., et al., 1992. Electrical resistivity tomography of vadose water movement. Water Resour. Res. 28 (5), 1429–1442. https://doi.org/10.1029/91WR03087.
Dickin, F., Wang, M., 1996. Electrical resistance tomography for process applications. Meas. Sci. Technol. 7 (3), 247. https://doi.org/10.1088/0957-0233/7/3/005.
Doi, A., Ejtemaei, M., Nguyen, A.V., 2019. Effects of ion specificity on the surface electrical properties of kaolinite and montmorillonite. Miner. Eng. 143, 105929. https://doi.org/10.1016/j.mineng.2019.105929.
Fan, Y., Yan, W., Xing, H., et al., 2025. Investigating petrophysical properties of gas hydrate-bearing sediments using digital rock technology: a microscopic perspective. Pet. Sci. 22 (5), 1889–1911. https://doi.org/10.1016/j.petsci.2025.02.010.
Fujii, T., Noguchi, S., Takayama, T., et al., 2013. In: Site Selection and Formation Evaluation at the 1st Offshore Methane Hydrate Production Test Site in the Eastern Nankai Trough, Japan. 75th EAGE Conference & Exhibition-Workshops. European Association of Geoscientists & Engineers. https://doi.org/10.3997/2214-4609.20131159.
Heeschen, K., Schicks, J., Oeltzschner, G., 2016. The promoting effect of natural sand on methane hydrate formation: grain sizes and mineral composition. Fuel 181, 139–147. https://doi.org/10.1016/j.fuel.2016.04.017.
Hu, G., Zhang, Z., Zhao, Y., et al., 2024. Formation mechanism and geophysical properties of fracture-filling gas hydrate in the host sediments: a comprehensive review. Earth Sci. Rev. 258, 104917. https://doi.org/10.1016/j.earscirev.2024.104917.
Jia, J., Tsuji, T., Matsuoka, T., 2016. Gas hydrate saturation and distribution in the Kumano Forearc Basin of the Nankai Trough. Explor. Geophys. 48 (2), 137–150. https://doi.org/10.1071/EG15127.
Jin, J., Wang, X., Deng, W., et al., 2025. Accumulation characteristics and occurrence differences of multitype gas hydrates in the northern South China Sea. Earth Sci. Front. 32 (2), 61–76. https://doi.org/10.13745/j.esf.sf.2024.11.19.
Johnson, A.H., 2011. Global Resource Potential of Gas Hydrate–A New Calculation.
Johnson, J.E., MacLeod, D.R., Phillips, S.C., et al., 2022. Primary deposition and early diagenetic effects on the high saturation accumulation of gas hydrate in a silt dominated reservoir in the Gulf of Mexico. Mar. Geol. 444, 106718. https://doi.org/10.1016/j.margeo.2021.106718.
Kelleher, B.P., Simpson, A.J., Rogers, R.E., et al., 2007. Effects of natural organic matter from sediments on the growth of marine gas hydrates. Mar. Chem. 103 (3–4), 237–249. https://doi.org/10.1016/j.marchem.2006.09.002.
Knackstedt, M., Arns, C., Sheppard, A., et al., 2007. Pore Scale Analysis of Electrical Resistivity in Complex Core Material. Proc of the Society of Core Analysts, Calgary, Canada.
Lan, X., Zou, C., Peng, C., et al., 2023. Uncertainty quantification in intelligent-based electrical resistivity tomography image reconstruction with Monte Carlo dropout strategy. IEEE Trans. Geosci. Rem. Sens. 61, 1–16. https://doi.org/10.1109/TGRS.2023.3262835.
Lee, M.W., Collett, T.S., 2006. A Method of Shaly Sand Correction for Estimating Gas Hydrate Saturations Using Downhole Electrical Resistivity Log Data. Scientific Investigations Report, pp. 2006–5121. https://doi.org/10.3133/sir20065121.
Lee, J.Y., Jung, J.W., Lee, M.H., et al., 2013. Pressure core based study of gas hydrates in the Ulleung Basin and implication for geomechanical controls on gas hydrate occurrence. Mar. Petrol. Geol. 47, 85–98. https://doi.org/10.1016/j.marpetgeo.2013.05.021.
Lei, L., Seol, Y., 2009. High-saturation gas hydrate reservoirs—A pore scale investigation of their formation from free gas and dissociation in sediments. J. Geophys. Res. Solid Earth 124 (12), 12430–12444. https://doi.org/10.1029/2019JB018243.
Lei, L., Seol, Y., Myshakin, E.M., 2019. Methane hydrate film thickening in porous media. Geophys. Res. Lett. 46, 11091–11099. https://doi.org/10.1029/2019GL084450.
Li, F., Sun, C., Li, S., et al., 2012. Experimental studies on the evolvement of electrical resistivity during methane hydrate formation in sediments. Energy Fuel. 26 (10), 6210–6217. https://doi.org/10.1021/ef301257z.
Li, Y., Wu, N., Liu, C., et al., 2022. Hydrate formation and distribution within unconsolidated sediment: insights from laboratory electrical resistivity tomography. Acta Oceanol. Sin. 41 (9), 127–136. https://doi.org/10.1007/s13131-021-1972-2.
Liang, J., Zhang, W., Lu, J., et al., 2019. Geological occurrence and accumulation mechanism of natural gas hydrates in the eastern Qiongdongnan Basin of the South China Sea: insights from site GMGS5-W9-2018. Mar. Geol. 418, 106042. https://doi.org/10.1016/j.margeo.2019.106042.
Liu, S., Han, T., Fu, L., 2023. Laboratory insights into the effects of methane hydrate on the anisotropic joint elastic-electrical properties in fractured sandstones. Pet. Sci. 20 (2), 803–814. https://doi.org/10.1016/j.petsci.2022.09.007.
Loke, M.H., Dahlin, T., 2002. A comparison of the Gauss–Newton and quasi-Newton methods in resistivity imaging inversion. J. Appl. Geophys. 49 (3), 149–162. https://doi.org/10.1016/S0926-9851(01)00106-9.
Lu, R., Stern, L.A., Du Frane, W.L., et al., 2019. The effect of brine on the electrical properties of methane hydrate. J. Geophys. Res. Solid Earth 124 (11), 10877–10892. https://doi.org/10.1029/2019JB018364.
Makogon, Y.F., 2010. Natural gas hydrates–A promising source of energy. J. Nat. Gas Sci. Eng. 2 (1), 49–59. https://doi.org/10.1016/j.jngse.2009.12.004.
McGinnis, D.F., Greinert, J., Artemov, Y., et al., 2006. Fate of rising methane bubbles in stratified waters: how much methane reaches the atmosphere? J. Geophys. Res., Oceans 111. https://doi.org/10.1029/2005jc003183.
Merritt, A., Chambers, J., Wilkinson, P., et al., 2016. Measurement and modelling of moisture—electrical resistivity relationship of fine-grained unsaturated soils and electrical anisotropy. J. Appl. Geophys. 124, 155–165. https://doi.org/10.1016/j.jappgeo.2015.11.005.
Metaxas, P.J., Lim, V.W., Booth, C., et al., 2019. Gas hydrate formation probability distributions: induction times, rates of nucleation and growth. Fuel 252, 448–457. https://doi.org/10.1016/j.fuel.2019.04.131.
Murray, H.H., 2007. Applied clay mineralogy: occurrences, processing and applications of kaolins, bentonites, palygorskitesepiolite, and common clays. Clays Clay Miner. 55 (6), 644–645. https://doi.org/10.1007/BF03406033.
Najafabadipour, A., Kamali, G.R., 2017. 3D Modeling and Bedrock Determination Using Electrical Resistivity Inversion. 23rd European Meeting of Environmental and Engineering Geophysics. European Association of Geoscientists & Engineers. https://doi.org/10.3997/2214-4609.201702108.
Perrone, A., Lapenna, V., Piscitelli, S., 2014. Electrical resistivity tomography technique for landslide investigation: a review. Earth Sci. Rev. 135, 65–82. https://doi.org/10.1016/j.earscirev.2014.04.002.
Pleasants, M., Neves, FdA., Parsekian, A., et al., 2022. Hydrogeophysical inversion of time-lapse ERT data to determine Hillslope Subsurface hydraulic properties. Water Resour. Res. 58 (4). https://doi.org/10.1029/2021WR031073.
Priegnitz, M., Thaler, J., Spangenberg, E., et al., 2013. A cylindrical electrical resistivity tomography array for three-dimensional monitoring of hydrate formation and dissociation. Rev. Sci. Instrum. 84 (10), 104502. https://doi.org/10.1063/1.4825372.
Priegnitz, M., Thaler, J., Spangenberg, E., et al., 2015. Characterizing electrical properties and permeability changes of hydrate bearing sediments using ERT data. Geophys. J. Int. 202 (3), 1599–1612. https://doi.org/10.1093/gji/ggv245.
Razafindratsima, S., Lataste, J.F., 2014. Estimation of the error made in pole–dipole electrical resistivity tomography depending on the location of the remote electrode: modeling and field study. J. Appl. Geophys. 100, 44–57. https://doi.org/10.1016/j.jappgeo.2013.10.008.
Riedel, M., Long, P., Collett, T.S., 2006. Estimates of *in situ* gas hydrate concentration from resistivity monitoring of gas hydrate bearing sediments during temperature equilibration. Mar. Geol. 227 (3–4), 215–225. https://doi.org/10.1016/j.margeo.2005.10.007.
Saidian, M., Godinez, L.J., Prasad, M., 2016. Effect of clay and organic matter on nitrogen adsorption specific surface area and cation exchange capacity in shales (mudrocks). J. Nat. Gas Sci. Eng. 33, 1095–1106. https://doi.org/10.1016/j.jngse.2016.05.064.
Seagar, A., Barber, D., Brown, B., 1987. Electrical impedance imaging. IEE Proc. A (Phys. Sci. Measure. Instrument.) 134 (2), 201–210. https://doi.org/10.1049/ip-a-1.1987.0028.
Shi, K., Wang, Z., Jia, Y., et al., 2022. Effects of the vertical heterogeneity on the gas production behavior from hydrate reservoirs simulated by the fine sediments from the South China Sea. Energy 255, 124525. https://doi.org/10.1016/j.energy.2022.124525.
Sloan Jr, E.D., 2003. Fundamental principles and applications of natural gas hydrates. Nature 426 (6964), 353–359. https://doi.org/10.1038/nature02135.
Sloan Jr, E.D., Koh, C.A., 2007. Clathrate Hydrates of Natural Gases. CRC press.
Spangenberg, E., Kulenkampff, J., 2006. Influence of methane hydrate content on electrical sediment properties. Geophys. Res. Lett. 33, l24315. https://doi.org/10.1029/2006GL028188.
Stanwix, P.L., Rathnayake, N.M., De Obanos, F.P., et al., 2018. Characterising thermally controlled CH_4–CO_2 hydrate exchange in unconsolidated sediments. Energy Environ. Sci. 11 (7), 1828–1840. https://doi.org/10.1039/C8EE00139A.
Su, M., Luo, K., Fang, Y., et al., 2021. Grain-size characteristics of fine-grained sediments and association with gas hydrate saturation in Shenhu Area, northern South China Sea. Ore Geol. Rev. 129, 103889. https://doi.org/10.1016/j.oregeorev.2020.103889.
Wang, X., Collett, T.S., Lee, M.W., et al., 2014. 2014. Geological controls on the occurrence of gas hydrate from core, downhole log, and seismic data in the Shenhu area, South China Sea. Mar. Geol. 357, 272–292. https://doi.org/10.1016/j.margeo.2014.09.040.
Wang, X., Liu, B., Qian, J., et al., 2017. 2017. Geophysical evidence for gas hydrate accumulation related to methane seepage in the Taixinan Basin, South China Sea. J. Asian Earth Sci. 168, 27–37. https://doi.org/10.1016/j.jseaes.2017.11.011.
Wedderburn, R.W., 1974. Quasi-likelihood functions, generalized linear models, and the Gauss—Newton method. Biometrika 61 (3), 439–447. https://doi.org/10.1093/biomet/61.3.439.
Wehrer, M., Slater, L.D., 2015. Characterization of water content dynamics and tracer breakthrough by 3-D electrical resistivity tomography (ERT) under transient unsaturated conditions. Water Resour. Res. 51 (1), 97–124. https://doi.org/10.1002/2014WR016131.
Wei, J., Fang, Y., Lu, H., et al., 2018. Distribution and characteristics of natural gas hydrates in the Shenhu Sea Area, South China Sea. Mar. Petrol. Geol. 98, 622–628. https://doi.org/10.1016/j.marpetgeo.2018.07.028.
Wiesenburg, D.A., Guinasso Jr, N.L., 1979. Equilibrium solubilities of methane, carbon monoxide and hydrogen in water and sea water. J. Chem. Eng. Data 24 (4), 356–360. https://doi.org/10.1021/je60083a006.
Xu, Z., Hu, T., Pang, X.Q., et al., 2022. Research progress and challenges of natural gas hydrate resource evaluation in the South China Sea. Pet. Sci. 19 (1), 13–25. https://doi.org/10.1016/j.petsci.2021.12.007.

Yin, Z., Chong, Z.R., Tan, H.K., Linga, P., 2016. Review of gas hydrate dissociation kinetic models for energy recovery. J. Nat. Gas Sci. Eng. 35, 1362–1387. https://doi.org/10.1016/j.jngse.2016.04.050.

Zhan, L., Kang, D., Lu, H., et al., 2022. Characterization of coexistence of gas hydrate and free gas using sonic logging data in the Shenhu Area, South China Sea. J. Nat. Gas Sci. Eng. 101, 104540. https://doi.org/10.1016/j.jngse.2022.104540.

Zhang, W., Liang, J., Lu, J., et al., 2017. Accumulation features and mechanisms of high saturation natural gas hydrate in Shenhu Area, northern South China Sea. Petrol. Explor. Dev. 44 (5), 708–719. https://doi.org/10.1016/S1876-3804(17)30082-4.

Zhao, G., Gong, G., Sun, H., et al., 2022. Effect of methane solubility on hydrate formation and dissociation: review and perspectives. Energy Fuel. 36 (14), 7269–7283. https://doi.org/10.1021/acs.energyfuels.2c01017.

Zhao, J., Liu, C., Li, C., et al., 2022. Pore-scale investigation of the electrical property and saturation exponent of Archie's law in hydrate-bearing sediments. J. Mar. Sci. Eng. 10 (1), 111. https://doi.org/10.3390/jmse10010111.

Zhu, Y., Yang, X., Huang, X., et al., 2024. Acoustic characterization of hydrate formation and decomposition in clay-bearing sediments. Pet. Sci. 21 (4), 2830–2838. https://doi.org/10.1016/j.petsci.2024.06.008.